



Calhoun: The NPS Institutional Archive
DSpace Repository

Theses and Dissertations

1. Thesis and Dissertation Collection, all items

2018-06

INFLUENCE OF ACCELERATION ON THE PATTERN AND DYNAMICS OF STRATIFIED WAKES

Guerrero, Rino M.

Monterey, CA; Naval Postgraduate School

<https://hdl.handle.net/10945/59671>

This publication is a work of the U.S. Government as defined in Title 17, United States Code, Section 101. Copyright protection is not available for this work in the United States.

Downloaded from NPS Archive: Calhoun



<http://www.nps.edu/library>

Calhoun is the Naval Postgraduate School's public access digital repository for research materials and institutional publications created by the NPS community. Calhoun is named for Professor of Mathematics Guy K. Calhoun, NPS's first appointed -- and published -- scholarly author.

Dudley Knox Library / Naval Postgraduate School
411 Dyer Road / 1 University Circle
Monterey, California USA 93943



NAVAL POSTGRADUATE SCHOOL

MONTEREY, CALIFORNIA

THESIS

**INFLUENCE OF ACCELERATION ON THE PATTERN
AND DYNAMICS OF STRATIFIED WAKES**

by

Rino M. Guerrero

June 2018

Thesis Advisor:
Second Reader:

Timour Radko
Justin M. Brown

Approved for public release. Distribution is unlimited.

THIS PAGE INTENTIONALLY LEFT BLANK

REPORT DOCUMENTATION PAGE			<i>Form Approved OMB No. 0704-0188</i>	
Public reporting burden for this collection of information is estimated to average 1 hour per response, including the time for reviewing instruction, searching existing data sources, gathering and maintaining the data needed, and completing and reviewing the collection of information. Send comments regarding this burden estimate or any other aspect of this collection of information, including suggestions for reducing this burden, to Washington headquarters Services, Directorate for Information Operations and Reports, 1215 Jefferson Davis Highway, Suite 1204, Arlington, VA 22202-4302, and to the Office of Management and Budget, Paperwork Reduction Project (0704-0188) Washington, DC 20503.				
1. AGENCY USE ONLY (Leave blank)	2. REPORT DATE June 2018	3. REPORT TYPE AND DATES COVERED Master's thesis		
4. TITLE AND SUBTITLE INFLUENCE OF ACCELERATION ON THE PATTERN AND DYNAMICS OF STRATIFIED WAKES			5. FUNDING NUMBERS W7B21	
6. AUTHOR(S) Rino M. Guerrero				
7. PERFORMING ORGANIZATION NAME(S) AND ADDRESS(ES) Naval Postgraduate School Monterey, CA 93943-5000			8. PERFORMING ORGANIZATION REPORT NUMBER	
9. SPONSORING / MONITORING AGENCY NAME(S) AND ADDRESS(ES) N/A			10. SPONSORING / MONITORING AGENCY REPORT NUMBER	
11. SUPPLEMENTARY NOTES The views expressed in this thesis are those of the author and do not reflect the official policy or position of the Department of Defense or the U.S. Government.				
12a. DISTRIBUTION / AVAILABILITY STATEMENT Approved for public release. Distribution is unlimited.			12b. DISTRIBUTION CODE A	
13. ABSTRACT (maximum 200 words) Submerged bodies traveling through stratified ocean columns generate remotely detectable wakes due to perturbations in temperature and momentum. Using the Massachusetts Institute of Technology General Circulation Model (MITgcm), a high-resolution 3D numerical ocean modeling program, simulations are run to model the quantitative and qualitative effects of a wake generated by accelerating submerged bodies. MITgcm was run on supercomputers at the University of Texas at Austin's Texas Advanced Computing Center and the Department of Defense High Performance Computing Modernization Program (HPCMP). The simulations modeled submerged bodies traveling at differing accelerating velocities or constant velocities. Wakes produced by accelerating bodies amplified the vorticity, thermal, and energy perturbation signatures. The stronger vortices concentrate the perturbations along the central wake, creating a narrower and more pointed wake front, whereas the wakes produced under constant velocity have weaker signatures, which are diffused across a broader wake front. The differences in wake signatures and wake shape can be detected using both acoustic- and non-acoustic-based methods and can be used operationally to determine the presence of acceleration within the incident submerged bodies.				
14. SUBJECT TERMS stratified wakes, MITgcm, internal velocity signatures, turbulence, acceleration			15. NUMBER OF PAGES 59	
			16. PRICE CODE	
17. SECURITY CLASSIFICATION OF REPORT Unclassified	18. SECURITY CLASSIFICATION OF THIS PAGE Unclassified	19. SECURITY CLASSIFICATION OF ABSTRACT Unclassified	20. LIMITATION OF ABSTRACT UU	

THIS PAGE INTENTIONALLY LEFT BLANK

Approved for public release. Distribution is unlimited.

**INFLUENCE OF ACCELERATION ON THE PATTERN AND DYNAMICS OF
STRATIFIED WAKES**

Rino M. Guerrero
Lieutenant, United States Navy
BS, University of California - Riverside, 2007

Submitted in partial fulfillment of the
requirements for the degree of

**MASTER OF SCIENCE IN METEOROLOGY AND PHYSICAL
OCEANOGRAPHY**

from the

**NAVAL POSTGRADUATE SCHOOL
June 2018**

Approved by: Timour Radko
Advisor

Justin M. Brown
Second Reader

Peter C. Chu
Chair, Department of Oceanography

THIS PAGE INTENTIONALLY LEFT BLANK

ABSTRACT

Submerged bodies traveling through stratified ocean columns generate remotely detectable wakes due to perturbations in temperature and momentum. Using the Massachusetts Institute of Technology General Circulation Model (MITgcm), a high-resolution 3D numerical ocean modeling program, simulations are run to model the quantitative and qualitative effects of a wake generated by accelerating submerged bodies. MITgcm was run on supercomputers at the University of Texas at Austin's Texas Advanced Computing Center and the Department of Defense High Performance Computing Modernization Program (HPCMP). The simulations modeled submerged bodies traveling at differing accelerating velocities or constant velocities. Wakes produced by accelerating bodies amplified the vorticity, thermal, and energy perturbation signatures. The stronger vortices concentrate the perturbations along the central wake, creating a narrower and more pointed wake front, whereas the wakes produced under constant velocity have weaker signatures, which are diffused across a broader wake front. The differences in wake signatures and wake shape can be detected using both acoustic- and non-acoustic-based methods and can be used operationally to determine the presence of acceleration within the incident submerged bodies.

THIS PAGE INTENTIONALLY LEFT BLANK

TABLE OF CONTENTS

I.	INTRODUCTION.....	1
A.	MOTIVATION	1
B.	BACKGROUND	1
C.	ACCELERATION.....	3
II.	METHODS	5
A.	NON-DIMENSIONALIZATION.....	5
B.	MODEL SETUP.....	6
III.	RESULTS	11
A.	VORTICITY	11
B.	THERMAL PERTURBATIONS	22
C.	WAKE AREA.....	26
D.	INTEGRATED ENERGY.....	29
IV.	DISCUSSION	35
A.	CONCLUSIONS	35
B.	OPERATIONAL RELEVANCE.....	36
C.	FUTURE RESEARCH.....	37
	LIST OF REFERENCES	39
	INITIAL DISTRIBUTION LIST	41

THIS PAGE INTENTIONALLY LEFT BLANK

LIST OF FIGURES

Figure 1.	Model Configuration for the Dynamic SB.....	7
Figure 2.	Vorticity Profile for Acc1	13
Figure 3.	Vorticity Profile for Acc2	14
Figure 4.	Vorticity Profile for Acc3	15
Figure 5.	Vorticity Profile for Con1	16
Figure 6.	Vorticity Profile for Con2.....	17
Figure 7.	Vorticity Profile for Con3.....	18
Figure 8.	Vorticity Profile for Con4.....	19
Figure 9.	Okubo-Weiss Parameter over Distance Traveled by SB	20
Figure 10.	Log ₁₀ of the Okubo Weiss Parameter over Reynolds Number	22
Figure 11.	Mask Configuration of the Model Volume.....	23
Figure 12.	Maximum Vertical T'_{RMS}	25
Figure 13.	Vertical Cross Section Configuration to Determine Wake Area	26
Figure 14.	Wake Area over SB Crossing Time ($t-t_{cross}$) for $T'_{RMS} > 1.0 \times 10^{-5}$	27
Figure 15.	Total Integrated Energy (E) over Distance Traveled (x_{SB})	30
Figure 16.	Energy Rate of Change over Reynolds Number.....	32
Figure 17.	Energy Decay over Time with Fitted Curves	33

THIS PAGE INTENTIONALLY LEFT BLANK

LIST OF TABLES

Table 1.	List of Simulations.....	9
Table 2.	OW Values across the Same Distance Traveled	21
Table 3.	Maximum T'_{RMS} Values	25
Table 4.	Wake Areas at SB Crossing and at Maximum.....	28
Table 5.	Integrated Energy Values across the Same Distance Traveled.....	31

THIS PAGE INTENTIONALLY LEFT BLANK

LIST OF ACRONYMS AND ABBREVIATIONS

Acc	Acceleration
ASW	Anti-Submarine Warfare
Con	Constant Velocity
Fr	Froude Number
MITgcm	Massachusetts Institute of Technology general circulation Model
Re	Reynolds Number
SB	Submerged Body
OW	Okubo-Weiss Parameter

THIS PAGE INTENTIONALLY LEFT BLANK

ACKNOWLEDGMENTS

Despite being a single project, this thesis includes the work and effort of many contributors. First my thanks goes to my thesis advisor, Dr. Timour Radko, whose initial work and creativity have guided the creation of this and several stratified wake projects. I would also like to thank Dr. Justin Brown, whose steady assistance helped correct my technical shortcomings and who provided the framework and troubleshooting for this thesis. Thank you to my predecessors, including Zach Moody, Michael Martin, Chris Merriam, Tom Newman, and Troy Benbow, for helping build the latest foundations of stratified wake research that this study is built upon. Thank you to my cohort, fellow METOC officers, classmates, and professors for making my NPS tour an enjoyable and memorable one.

My greatest thanks goes to my family. My wife, Sarah; daughter, Clara; and son, Reid; who greeted me with smiles and grins every day when I came back home to them. Their presence has grounded me and kept me focused on what is truly important: to work hard to complete this study and return to them. My gratitude also extends to my parents, Ricardo and Nora; brother, Eric; my parents-in-law, Rocky and Sherri; and brother- and sister-in-law, Christian and Christie; for visiting, helping with the little ones, and reminding us that we live in beautiful Monterey and we should go enjoy the area.

THIS PAGE INTENTIONALLY LEFT BLANK

I. INTRODUCTION

A. MOTIVATION

Anti-Submarine Warfare (ASW), which is a critical component of all navies, has been made increasingly difficult by the adoption of new technologies such as air-independent propulsion systems and noise-reducing outer tiles and skins. Submarine hunters and trackers must constantly improve undersea detection technologies, using new sensor platforms, such as satellites and unmanned underwater vehicles, and new detection methods. Wake detection is an interesting hybrid of traditional acoustic and non-acoustic submarine detection methods. Rather than directly measure acoustic signatures such as submarine machinery or water flow across the hull, one can instead detect the wake signatures themselves acoustically. Additionally, wakes can be detected non-acoustically, through visual, thermal, and radar-based means. Wake detection is an exciting field of study for the ASW community, as this field can theoretically counter continued advances in submarine acoustic noise reduction.

To further the field of wake detection, this study seeks to advance the current understanding of wake behavior in stratified fluids such as the ocean. Rather than employing expensive and often data constrained field experiments, this study uses direct numerical simulations (DNS), a more cost effective and practical method to study stratified wake behavior. This thesis focuses on the simulated behavior of stratified wakes produced by accelerating and non-accelerating submerged bodies with a particular emphasis on the wake signatures most likely to be used for wake detection.

B. BACKGROUND

Submerged bodies (SB) propagating through stratified water columns transfer momentum to the surrounding fluid to generate wakes. These fluid flows are often described using two dimensionless quantities, the Reynolds number (Re) and the Froude number (Fr), defined as follows:

$$Re = \frac{UL}{\nu}, \quad (1.1)$$

$$Fr = \frac{U}{NL}. \quad (1.2)$$

These quantities portray the relationship between the SB velocity U , the SB diameter L , the kinematic viscosity ν of the fluid, and the Brunt-Väisälä or buoyancy frequency (N), which is defined as

$$N = \sqrt{-\left(\frac{g}{\rho_0}\right)\left(\frac{\partial \rho}{\partial z}\right)}, \quad (1.3)$$

where g is the gravitational acceleration, ρ_0 is a reference density, ρ is the density of the fluid, z is the depth.

The Reynolds number is the ratio of inertial forces to viscous forces. Unstratified experiments, such as those by Pao and Kao (1977), show a wide range of phenomena across varying values of Re . At small Re , viscous forces dominate, and there is laminar wake flow around the incident body. As Re increases, the laminar flow becomes unstable and von Kármán vortex streets begin to form, shedding regular eddies in its lee. At even higher Re , the vortex street structure breaks down, and the wake flow becomes turbulent. Within stratified water columns, where density increases with depth, the stratification is perturbed by the presence of turbulent flows. In kind, the stratification exerts a gravitational restoring force on these perturbations, which leads to the generation of internal waves (Lin and Pao 1979). In substantially turbulent regimes, the fluid perturbations can create long-lasting wake signatures as the restoring force tends to result in the collapse of these wakes into flattened structures. In contrast, the wake signatures in homogenous fluids are only composed of velocity signatures, where the wake does not experience wake collapse and so tends to be weaker and diffuse faster (Schooley and Stewart 1963).

Typical studies of stratified wakes identify three characteristic stages of wake development: the near, intermediate, and late wakes. The initial two stages can be described with the Froude number, which measures the ratio of the inertial force to the buoyancy force (see, for example, the review by Lin and Pao 1979). After the initial passage of a high velocity SB and turbulent mixing, there is a high Fr near-wake region growing in three dimensions (Spedding 2002). The inertial forces are sufficiently high to overcome buoyancy forces and the wake grows both horizontally and vertically with examples

presented in Redford et al. (2015). In the intermediate wake as decay initiates, the Fr is decreasing and the buoyancy term begins to assert itself where the vertical velocities are cancelled by the buoyancy forces, and the flow shape collapses into flat horizontal vortices (Meunier and Spedding 2004). The late wake describes the dissipation of the smaller perturbations and the creation of persistent late-wake structures. These structures exhibit high degrees of order and coherence that correspond to higher velocities of the incident bodies (Spedding 1997).

Advances in supercomputers in recent years have allowed DNS methods to come to the forefront of the field. DNS allow for focused, quantitative studies that can easily isolate the effects of select fluid properties. Recent research has identified the strongest wake signatures for possible use in wake detection. Particular diagnostics include thermal and momentum signatures at the surface (Newman 2014) and at depth (Merriam 2015, Martin 2016; Benbow 2016; Moody et al. 2016), which established that increased SB speed, depth, and size are associated with increased wake signature occurrence and strength. These signatures were found to persist for several days, suggesting that such diagnostics can be a viable method of non-acoustic detection of submerged bodies (Benbow 2016). Vorticity-based signatures are another viable detection diagnostic, as they can persist for several days and late wake pancake vortices develop distinct crescent shapes over time when under the effects of Coriolis (Lorfeld 2017). Recent numerical and fieldwork addresses the wake signatures produced by SBs with constant velocities but do not address the effects of acceleration.

C. ACCELERATION

Voropayev, et al. (1999) previously hypothesized that SBs under the effects of turning and acceleration would lead to the amplification of interior and surface wake signatures. This is under the basis of the added mass effect first proposed by Bessel (1828), as the SB accelerates there needs to be an increasing amount of fluid to be displaced as the SB propagates through the volume. This causes a growing upstream wake, the region of displaced fluid ahead of the propagating SB (Mitkin and Chashechkin 2000). Acceleration increases the size of upstream wake, adding a growing amount inertia to the system, and

increasing the Re . Correspondingly, the wake enters more turbulent regimes, and ultimately the wake signatures are amplified as compared to signatures produced by a SB propagating under constant velocity.

Using DNS of a spherical body accelerating in a stratified fluid, this study examines the effects of accelerating SBs on the persistent wake signatures of temperature and vorticity. This study is the first comprehensive investigation of this hypothesis in the context of submersibles. Two key wake signatures for potential use in wake detection are focused on in this study, the thermal perturbations and the presence of pancake vortices. Section II of the study, describes the model configuration, and assumptions. Section III, presents the results of the vorticity, thermal, and energy based diagnostics. And Section IV poses the conclusions, operational relevance and future research opportunities of the study.

II. METHODS

A. NON-DIMENSIONALIZATION

For these simulations, the system is assumed to satisfy the Boussinesq approximations, is incompressible, experiences no external rotation, and has uniform salinity. The DNS methods simulate fluid flows by solving the Navier–Stokes equations under these assumptions, which are given by:

$$\nabla \cdot \mathbf{u}^* = 0, \quad (2.1)$$

$$\frac{\partial T^*}{\partial t^*} + \mathbf{u}^* \cdot \nabla T^* = \kappa_T \nabla^2 T^*, \quad (2.2)$$

$$\rho_0 \left(\frac{\partial \mathbf{u}^*}{\partial t^*} + \mathbf{u}^* \cdot \nabla \mathbf{u}^* \right) = -\nabla p^* + \rho_0 \alpha T^* g \hat{\mathbf{e}}_z + \rho_0 \nu \nabla^2 \mathbf{u}^*. \quad (2.3)$$

Where \mathbf{u}^* is the velocity, T^* is the temperature, t^* is time, κ_T is the temperature diffusivity, p^* is the pressure, α is the coefficient of thermal expansion (assumed constant), g is the gravitational acceleration, $\hat{\mathbf{e}}_z$ is the unit vector in the vertical direction, and ν is the kinematic viscosity. The stars are used to differentiate between dimensional (starred) and non-dimensional (un-starred) quantities. In order to conveniently scale the results to a variety of submerged body length scales, the aforementioned equations are non-dimensionalized. The unit of length is the diameter of the spherical submerged object, L . The units of time, temperature, and pressure are given as follows:

$$[t] = \sqrt{\frac{L}{g}}, \quad (2.4)$$

$$[T] = \frac{1}{\alpha}, \quad (2.5)$$

$$[p] = \rho_0 L g. \quad (2.6)$$

To perform the non-dimensionalization, the two non-dimensional quantities for the thermal diffusivity and kinematic viscosity are given by

$$\kappa_{T,\text{nd}} = \kappa_T g^{-\frac{1}{2}} L^{\frac{3}{2}}, \quad (2.7)$$

$$\nu_{\text{nd}} = \nu g^{-\frac{1}{2}} L^{\frac{3}{2}}. \quad (2.8)$$

The non-dimensionalized governing equations for continuity, temperature, and momentum are respectively given by

$$\nabla \cdot \mathbf{u} = 0, \quad (2.9)$$

$$\frac{\partial T}{\partial t} + \mathbf{u} \cdot \nabla T = \kappa_{T,\text{nd}} \nabla^2 T, \quad (2.10)$$

$$\frac{\partial \mathbf{u}}{\partial t} + \mathbf{u} \cdot \nabla \mathbf{u} = -\nabla p + T \mathbf{e}_z + \nu_{\text{nd}} \nabla^2 \mathbf{u}. \quad (2.11)$$

For the purposes of presenting results, dimensional and non-dimensional quantities are given. For the dimensional results, representative values are chosen for the various parameters of the system: the thermal expansion coefficient is set to 0.000214 K^{-1} , g is set to 9.8 m/s^2 , and L is set to 10 m . The dimensional equivalents of the non-dimensional results are provided in parentheses throughout this paper.

B. MODEL SETUP

The Massachusetts Institute of Technology General Circulation Model (MITgcm) was chosen for the experiment, as it is a non-hydrostatic ocean model able to resolve small-scale features efficiently through parallel processing (Marshall et al., 1997). The simulations, data output processing, and data storage for this study were conducted across four supercomputer systems: The University of Texas at Austin's Texas Advanced Computing Center's Stampede2 (a Dell PowerEdge cluster) and the Department of Defense (DOD) Shared Resource Center's High Performance Computing Modernization Program's Onyx (XC40/50), Conrad (Cray XC40), Excalibur (Cray XC40), and Garnet (Cray XE6) supercomputers. The results were transferred to and further analyzed on Naval Postgraduate School (NPS) computer systems.

The model simulates a SB being towed through the center of a rectangular fluid-filled box to produce the wakes. Additional simulations were conducted with a static SB with a background flow applied to produce the wakes, and similar results were achieved but are not discussed further in this study. A diagram of the model configuration is depicted in Figure 1. To optimize computational efficiency, 200 point exponential grids were arrayed along the y - and z -axes, with the highest resolutions of $\Delta y = \Delta z = .0131$ (.131 m)

near the submerged body's axis of travel at the box's center and the lowest resolutions $\Delta y = \Delta z = .1277$ (1.277 m) located along the outer perimeters of the box, for a total length of 10 units (100 meters) in y and z . The x -axis used a uniformly spaced 3,200-point grid with $\Delta x = .01$ (.1 meters), for a total length of 32 units (320 meters). This constant high resolution throughout the propagation path allows for the same model resolution of the early, intermediate and decaying wakes. The top, bottom, fore and aft ends of the box are impermeable free-slip boundaries. The sidewalls are periodic boundaries. The top, bottom, and sidewalls are placed sufficiently far to prevent their influence on the interior wake. The fluid is initially at rest until perturbed by the SB. The volume has an initial vertical temperature gradient (T_{0z}) with $+1 \times 10^{-2}$ temperature deviation from the mean toward the top and -1×10^{-2} temperature deviation toward the bottom. The kinematic viscosity ν_{nd} and the thermal diffusivity are both set to 1×10^{-4} .

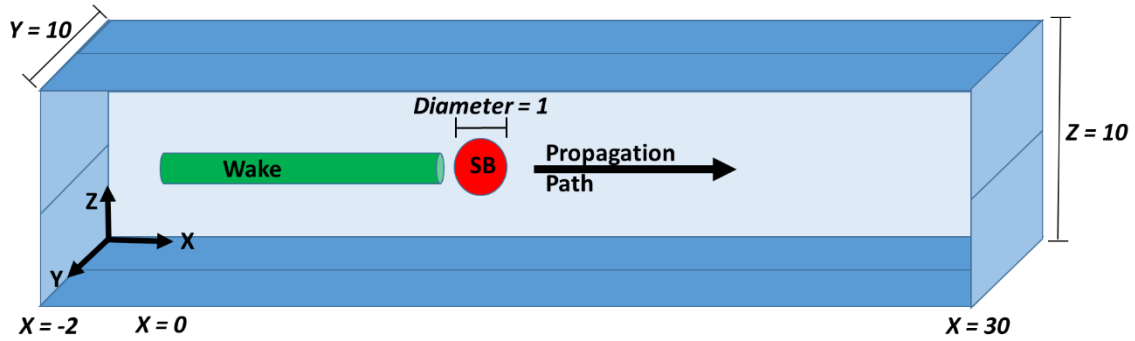


Figure 1. Model Configuration for the Dynamic SB

The simplest shape for the study, a sphere, was chosen for the SB. The fluid flows around bluff bodies such as a sphere exhibit higher magnitudes of wake signatures in the near and intermediate wakes as compared to more ellipsoidal shapes (Spedding 2014), which is particularly helpful in our study to isolate the effects of acceleration. Late wakes do not show a strong dependence on the geometry of the SB (Spedding 2014), so these results should be applicable to many similar geometries.

To begin, the SB center is placed two sphere diameters (20 m) away from the back edge of the box. The SB travels horizontally along the x -axis through the center of the box until just before the SB encounters the box edge. The SB is towed either with a constant acceleration a or a constant velocity u_0 . For the accelerating cases, a takes the values .005 ($.05 \text{ m/s}^2$) for case Acc1, .01 ($.1 \text{ m/s}^2$) for case Acc2, and .002 ($.2 \text{ m/s}^2$) for case Acc3. For the constant velocity cases, the velocity of the SB takes the values $u_0 = .1925$ (1.91 m/s) for case Con1, .385 (3.81 m/s) for case Con2, .5775 (5.72 m/s) for case Con3, and .770 (7.62 m/s) for case Con4. The constant velocities were chosen to be approximately the $\frac{1}{4}$ proportion intervals of the maximum velocity achieved by case Acc2 upon reaching end of the model volume. Thus, the SB in Con2 travels across the volume at approximately the mean velocity for the Acc2 case. To study the effects of wake decay in greater detail, Acc2 and Con2 were continued after the passage of the SB. All simulations are summarized in Table 1.

Table 1. List of Simulations

Case Name	Acceleration of SB	Constant Velocity of SB	Run Time ¹ (s)	Final Velocity of SB in Box	Mean Velocity of SB in Box	Maximum <i>Fr</i>	Run Time with decay ² (s)
Acc1	0.005 (.05m/s ²)		108	.54 (5.35 m/s)	.27 (2.67 m/s)	11.67	
Acc2	0.01 (.1m/s ²)		76	.76 (7.52 m/s)	.38 (3.76 m/s)	16.43	130
Acc3	0.02 (.2m/s ²)		54	1.08 (10.69 m/s)	.54 (5.35 m/s)	23.35	
Con1		0.1925 (1.91 m/s)	155		.1925 (1.91 m/s)	4.16	
Con2		0.385 (3.81 m/s)	76		.385 (3.81 m/s)	8.32	117
Con3		0.5775 (5.72 m/s)	51		.5775 (5.72 m/s)	12.48	
Con4		0.77 (7.62 m/s)	38		.77 (7.62 m/s)	16.65	

1. Time for SB to transit across and before exiting the model volume.

2. Total model run time including after the SB has left the model volume to allow for study of wake decay.

Normalized units are placed in parentheses and are calculated using $L = 10$, $g = 9.8$, and $\nu = .003$.

THIS PAGE INTENTIONALLY LEFT BLANK

III. RESULTS

A. VORTICITY

For the purposes of detecting wakes using vortices, it is reasonable to investigate the presence, distribution, and amount of vorticity given differing accelerations and constant velocities. The wake's vertical vorticity (ω) is expressed as

$$\omega = \frac{\partial v}{\partial x} - \frac{\partial u}{\partial y}. \quad (3.1)$$

Where u is the horizontal velocity along the x -axis and v is the horizontal velocity along the y -axis. To isolate the vorticity from the strain present in the system, the Okubo-Weiss parameter (OW) is used for this study's quantitative vorticity measurements. The Okubo-Weiss parameter and its normal strain (s_n) and shear strain (s_s) components are defined as:

$$OW = s_n^2 + s_s^2 - \omega^2, \quad (3.2)$$

$$s_n = \frac{\partial u}{\partial x} - \frac{\partial v}{\partial y}, \quad (3.3)$$

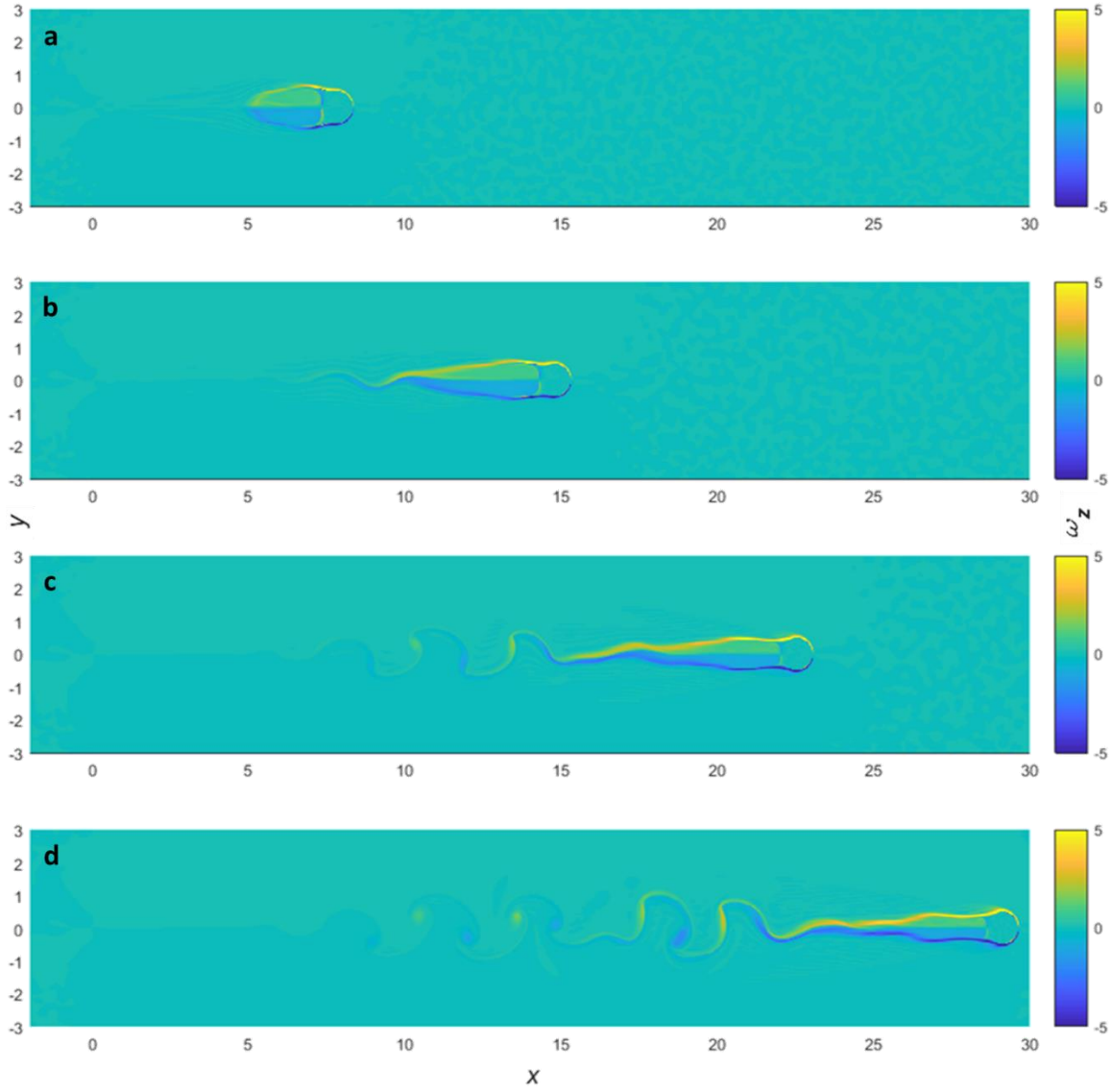
$$s_s = \frac{\partial v}{\partial x} + \frac{\partial u}{\partial y}. \quad (3.4)$$

This parameter differentiates between vorticity due to eddies and vorticity due to shear, with shear-dominated systems having positive OW and eddy-dominated systems having negative OW (Vortmeyer-Kley et al. 2016). For the purposes of this study, only the negative OW values were included in the analysis.

To identify the qualitative properties of the wakes, the vorticity fields downstream of the SB are first investigated. Horizontal cross sections of the vorticity profiles (ω) are taken at the center of the model volume and are plotted in Figures 2-4 for the accelerating SB cases, and in Figures 5-8 for the constant velocity SB cases. Each figure depicts a time series of the SB propagating along the x -axis at approximately $\frac{1}{4}$ intervals (75m) of the total travel length until just before the SB contacts the terminal edge of the model volume. For the accelerating cases, the wake initially develops as a laminar flow with an increasing diameter wake immediately behind the SB, best seen in Figure 2a. In Figure 2b at $Re \approx 2,400$, the wake begins to narrow. In Figures 2c-d at Re above 3,400, the wake tail begins

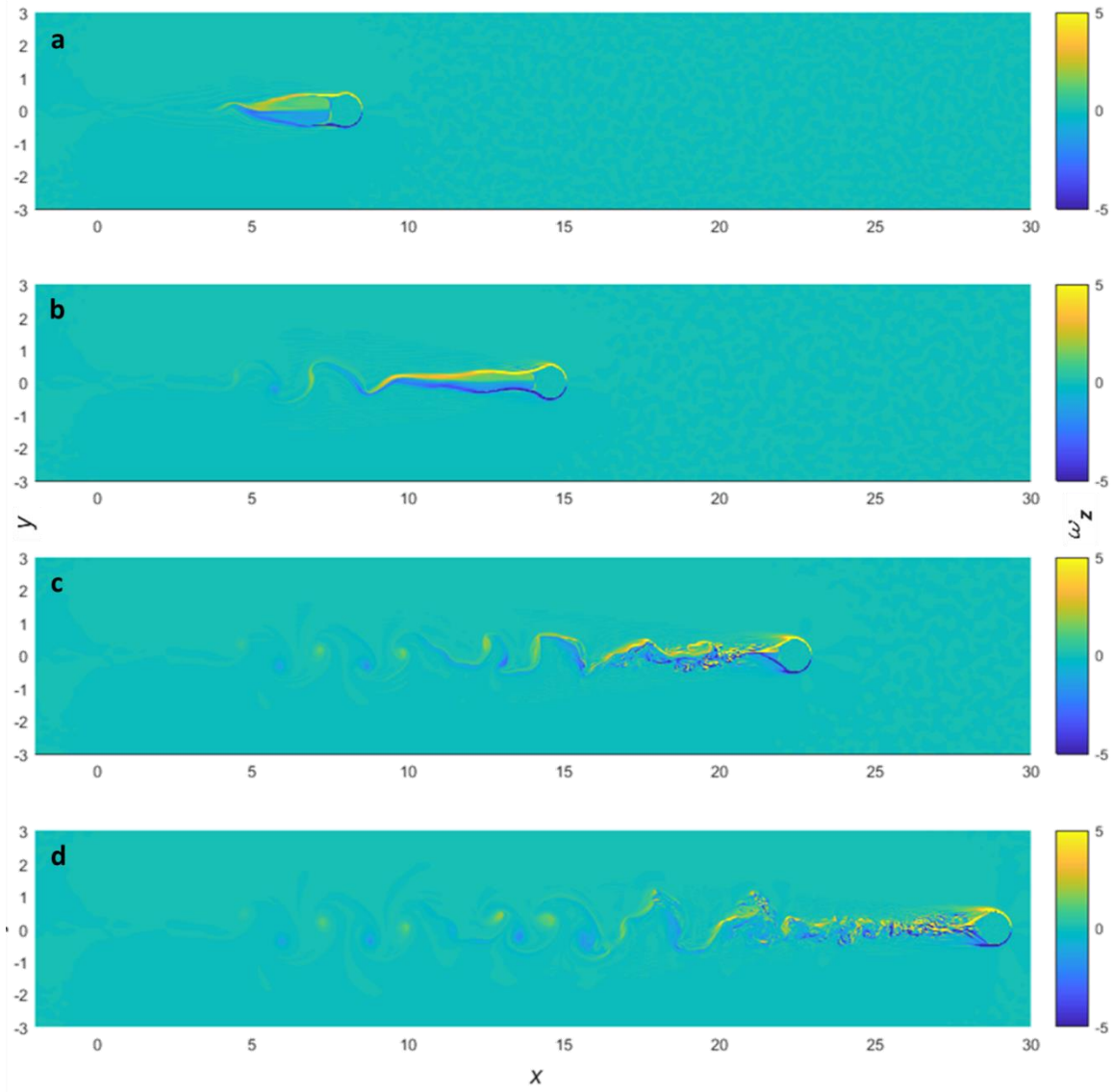
to develop sinusoidal behavior, leading to the creation of eddies in the coherent wake, and the formation of von Kármán vortex streets. Additionally, in Figures 2d and 3b, the wake diameter continues to decrease until a split three-part wake develops, composed of two lateral wakes and one middle wake. This three-part wake is more evident in Figure 3c at $Re \approx 5,000$, where the middle wake diameter further decreases and the lateral wakes increase in length until they start vortex shedding. In Figure 4c at $Re \approx 7,600$, the middle wake collapses and separates from the surface of the SB. The near wake immediately behind the SB becomes fully turbulent and is dominated by the formation of eddies. In Figures 4b–d, as Re increases the number of vortices produced by the wake similarly increases. This effect widens the fully turbulent region in the near wake from a thin strand centered behind the SB, to the width of the SB

Fully turbulent flow is achieved in two of the accelerating cases, Acc2 (Figure 3) and Acc3 (Figure 4), and two of the constant velocity cases, Con3 (Figure 7) and Con4 (Figure 8), which leads to the development of eddies. The slower moving Acc1 (Figure 2), Con1 (Figure 6), and Con2 (Figure 7) develop von Kármán vortex streets but do not achieve fully turbulent wake flow. Comparing Acc2 and its mean velocity counterpart, Con2, the accelerating case has more and stronger eddies than the constant velocity case across the same distance and time traveled. The narrow formation of eddies behind the SB of Acc2 (Figure 3d) are in a tighter formation around the propagation axis, are more numerous, and display greater vorticity than those in Con2 (Figure 6d).



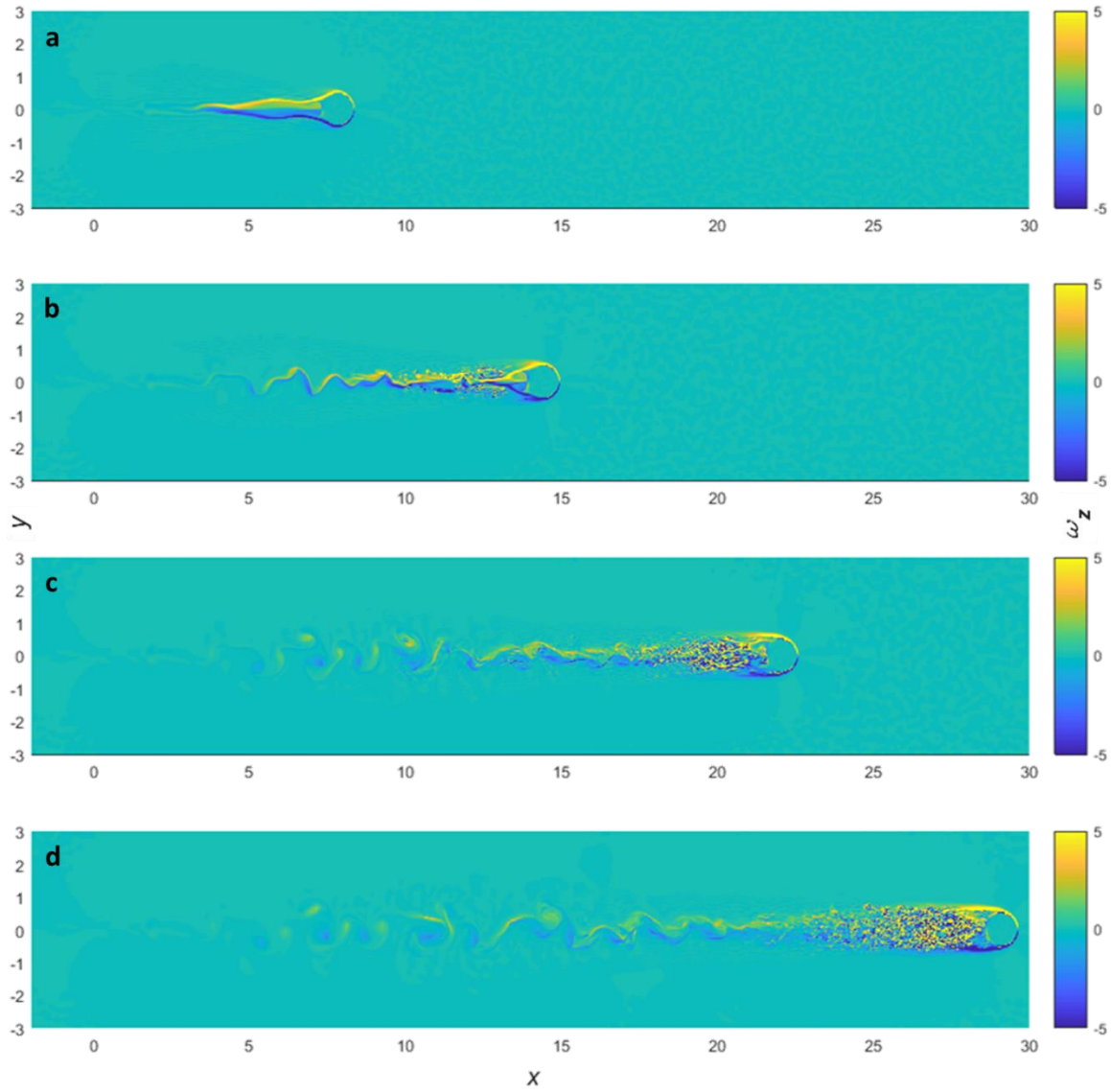
The horizontal cross sections are taken at times 56 (a), 77 (b), 95 (c), and 109 (d). The profile is zoomed in to focus on the central propagation axis and the colorbar is rescaled to show the smaller details.

Figure 2. Vorticity Profile for Acc1



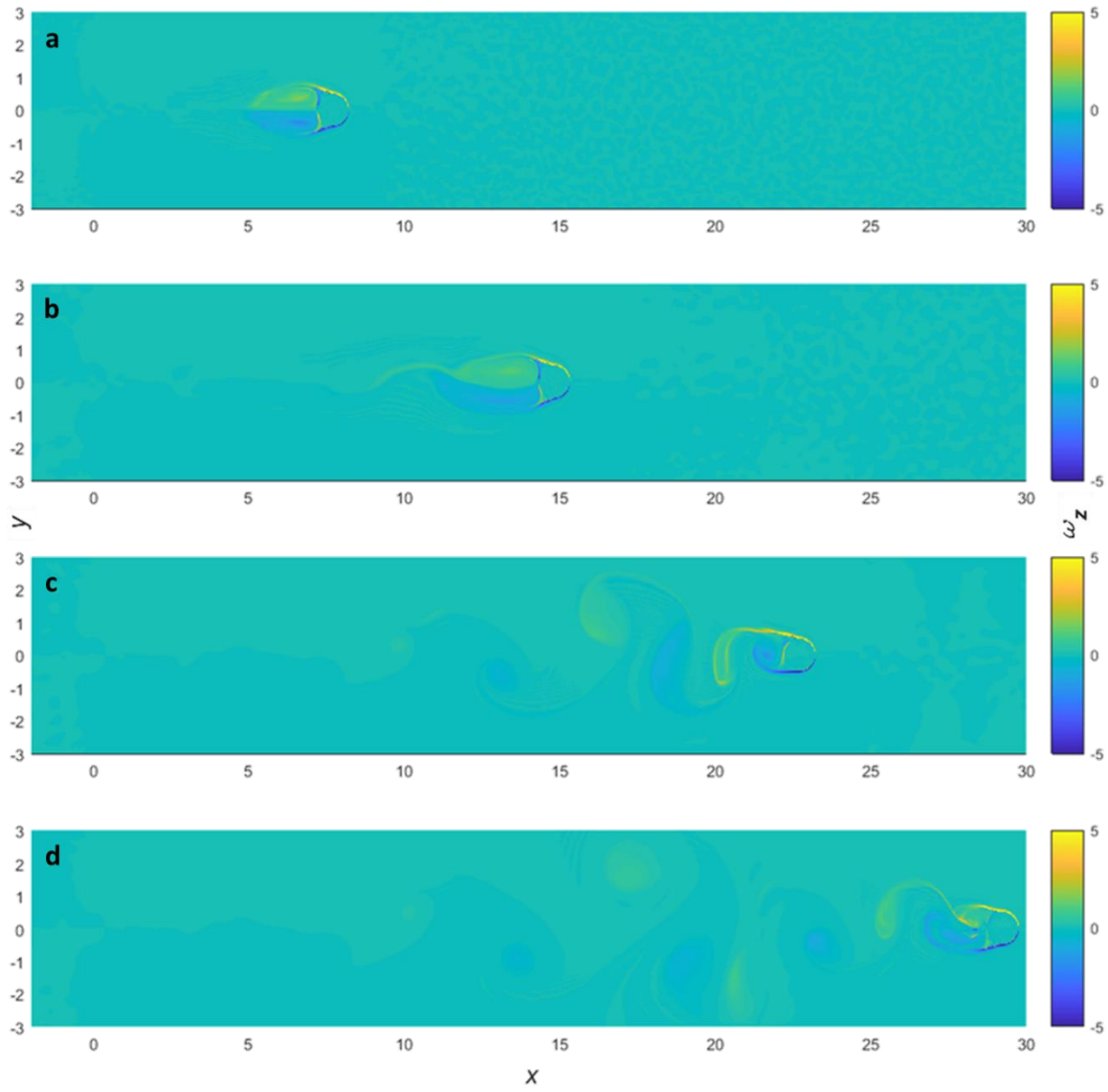
The horizontal cross sections are taken at times 40 (a), 54 (b), 67 (c), and 76 (d). The profile is zoomed in to focus on the central propagation axis and the colorbar is rescaled to show the smaller details.

Figure 3. Vorticity Profile for Acc2



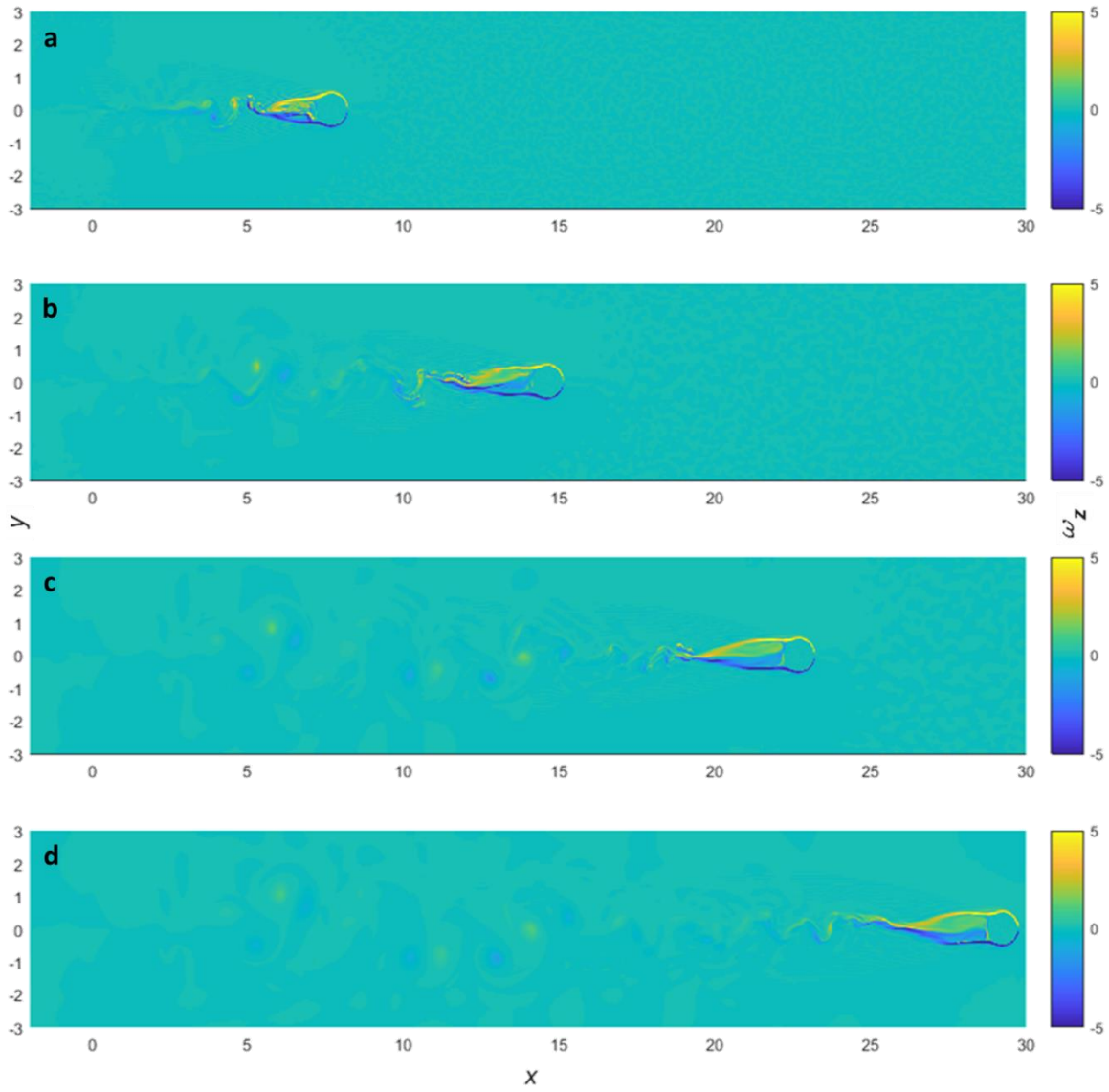
The horizontal cross sections are taken at times 28 (a), 38 (b), 47 (c), and 54 (d). The profile is zoomed in to focus on the central propagation axis and the colorbar is rescaled to show the smaller details.

Figure 4. Vorticity Profile for Acc3



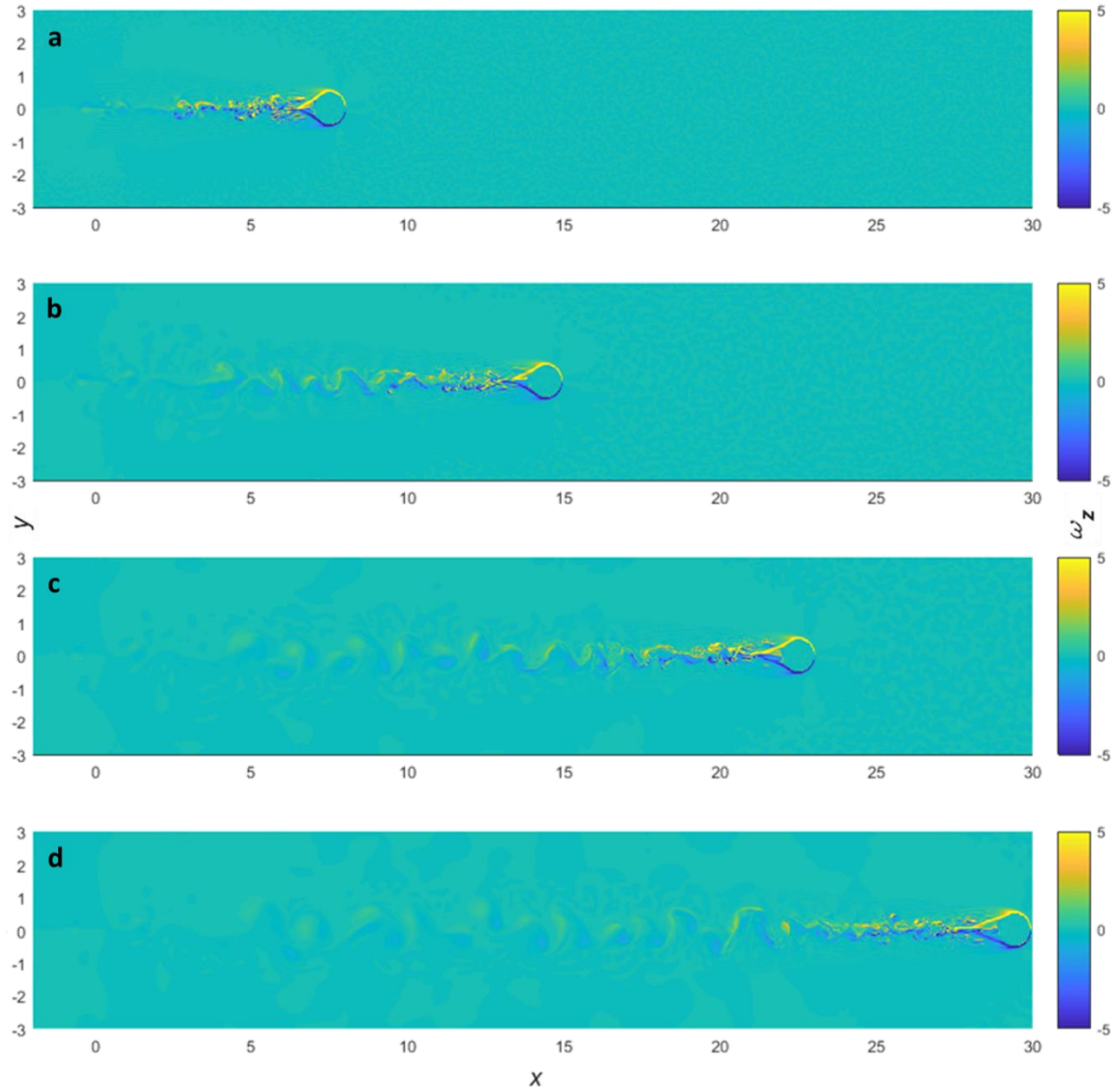
The horizontal cross sections are taken at times 41 (a), 77 (b), 119 (c), and 155 (d). The profile is zoomed in to focus on the central propagation axis and the colorbar is rescaled to show the smaller details.

Figure 5. Vorticity Profile for Con1



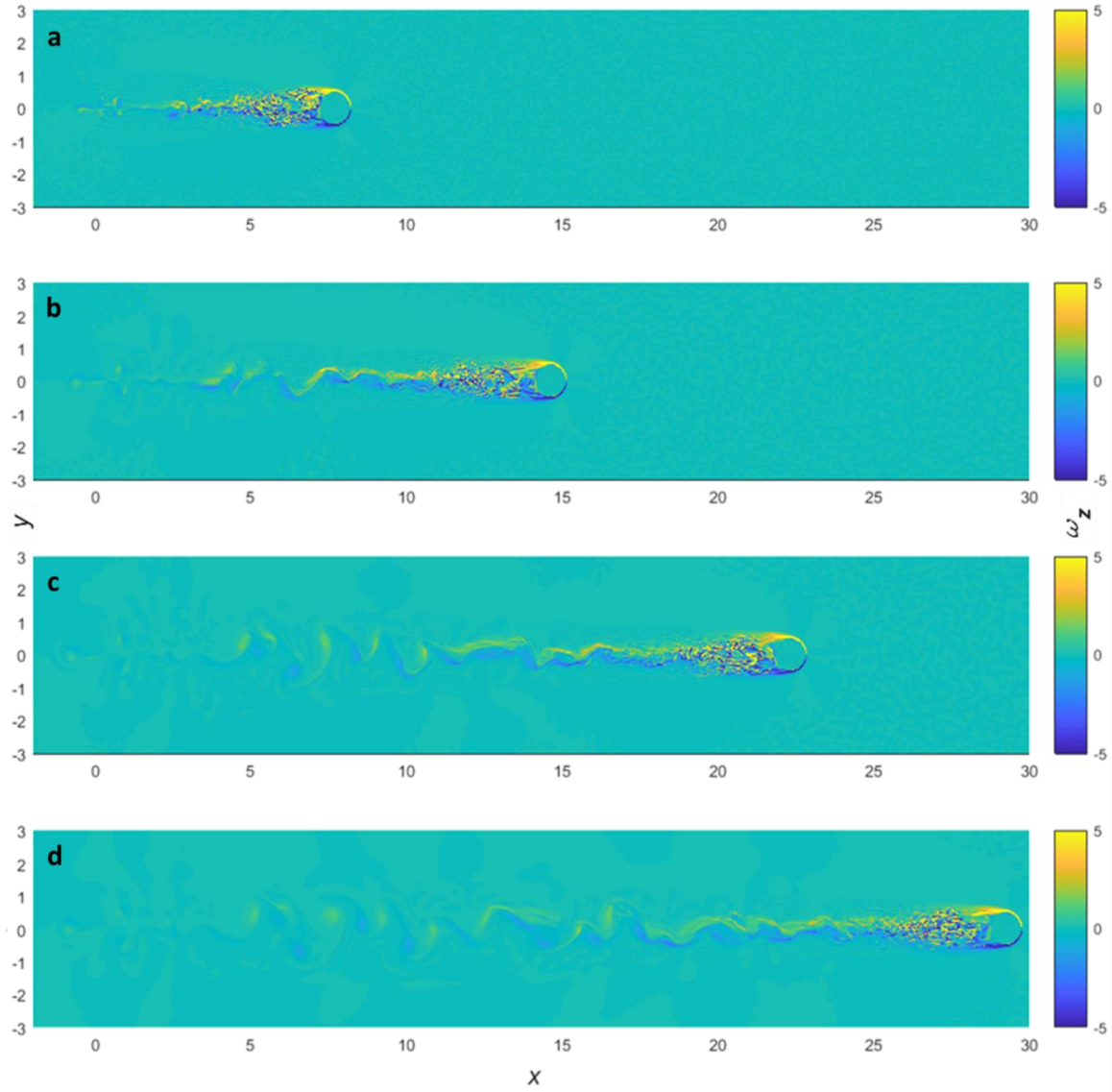
The horizontal cross sections are taken at times 20 (a), 38 (b), 59 (c), and 76 (d). The profile is zoomed in to focus on the central propagation axis and the colorbar is rescaled to show the smaller details.

Figure 6. Vorticity Profile for Con2



The horizontal cross sections are taken at times 13 (a), 25 (b), 39 (c), and 51 (d). The profile is zoomed in to focus on the central propagation axis and the colorbar is rescaled to show the smaller details.

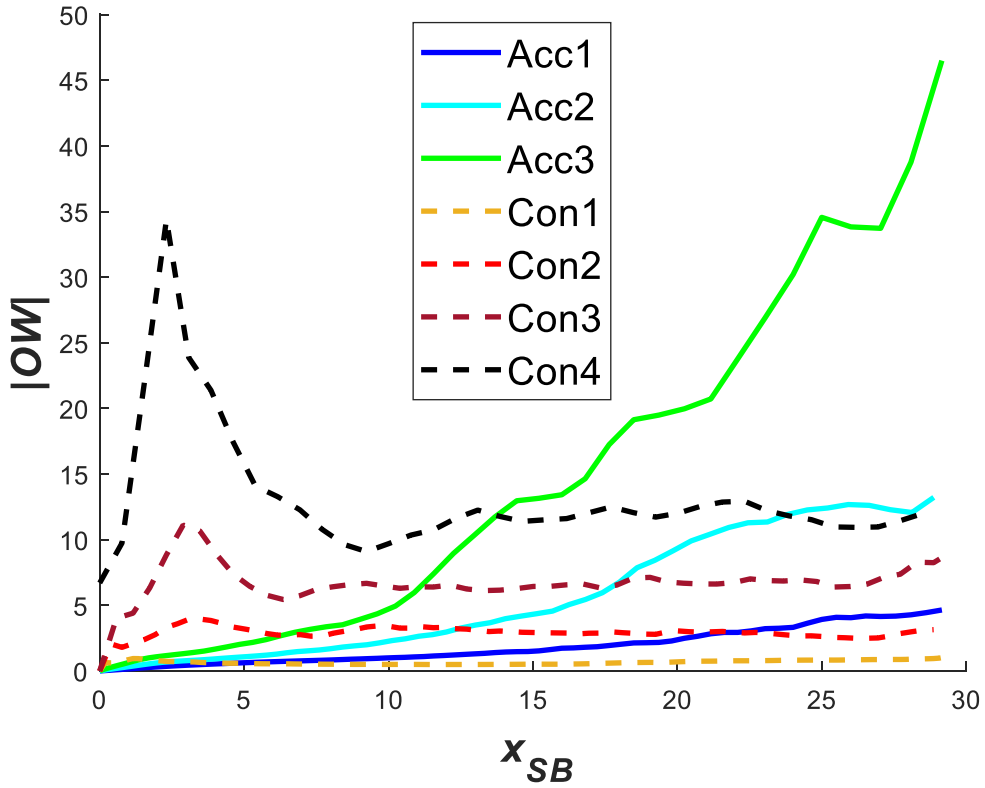
Figure 7. Vorticity Profile for Con3



The horizontal cross sections are taken at times 10 (a), 19 (b), 29 (c), and 38 (d). The profile is zoomed in to focus on the central propagation axis and the colorbar is rescaled to show the smaller details.

Figure 8. Vorticity Profile for Con4

To quantify the total presence of vortices in the SB wake, OW was integrated across the model volume and plotted for different values of Re in Figure 9. The maximum OW values achieved by the cases after having traveled 30 (300m) are listed in Table 2. In the constant velocity cases after the initial transients, OW reaches a steady state, when the amounts of OW generation and decay have achieved an equilibrium. Across the same distance traveled at $x = 30$, the Acc cases exhibit higher OW than their respective Con counterparts. This is especially evident for the Acc2 case, where Acc2's OW is 4.2 times larger than the OW of Con2. And Acc2 has slight more but comparable OW than Con4, despite only traveling at similar velocities of .77 (7.62m/s) for a short period of time.



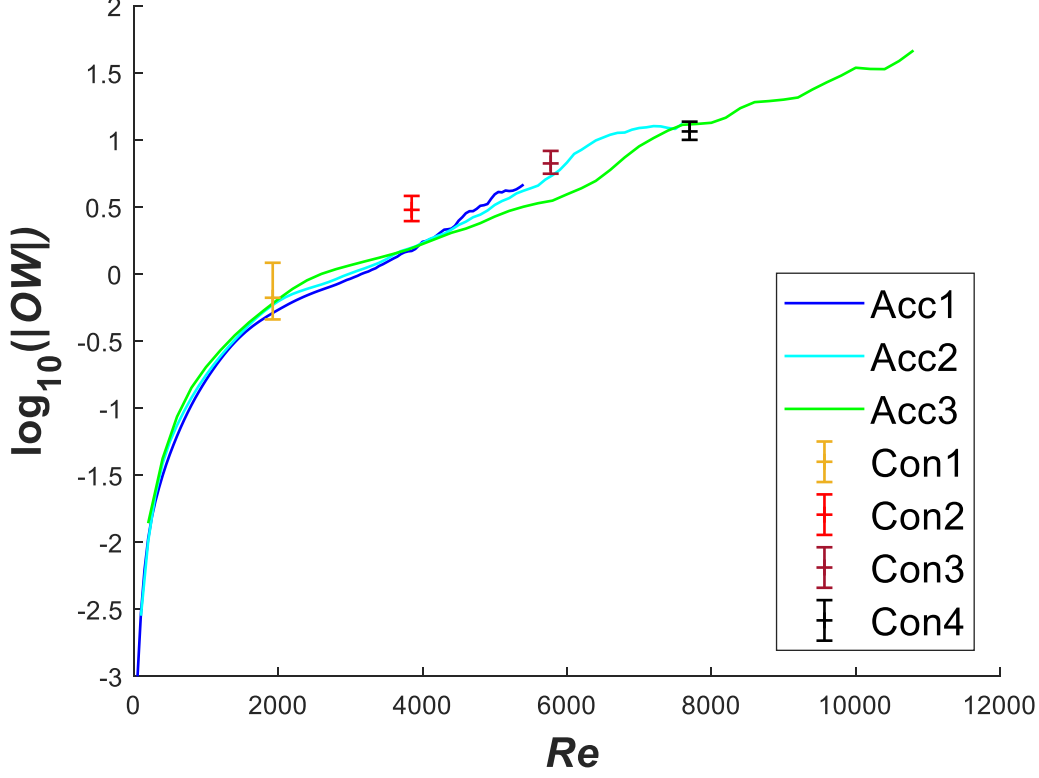
The initial values for the Con simulations were removed due to the initial high OW values created by the SB transitioning from rest to their set velocities.

Figure 9. Okubo-Weiss Parameter over Distance Traveled by SB

Table 2. OW Values across the Same Distance Traveled

Simulation	Acc1	Acc2	Acc3	Con1	Con2	Con3	Con4
OW at $x \approx 30$	4.65	13.23	46.49	1.06	3.15	9.03	11.99

To further investigate the OW values in relation to Re , the OW are plotted over Re , using instantaneous values for the Acc cases and the time averages of the Con cases (with the startup transients excised) in Figure 10. The fluctuations in OW generation and decay for the Con cases are represented as two standard deviation tall error bars about a mean $\log_{10}(OW)$. Upon reaching the same Re for Con1–3, the Acc cases have lower but fairly comparable OW . This is attributed to the fact that the constant velocity SBs have been traveling larger velocities for a more extended time and have therefore been producing eddies with a high OW for much longer than the Acc cases. In contrast, at Con4’s Re , Acc2 and Acc3 have achieved slightly higher but still fairly similar OW values. This can be attributed to two factors: the generation of stronger and more persistent eddies with a correspondingly weaker decay rate at the more turbulent fluid regimes. Second, the differences in OW at higher Re in the fully turbulent regimes are relatively minor. Hence, the Acc2 and Acc3 cases have been traveling at a similar OW generating turbulent regime as the higher Con4. Thus, OW is largely a function of Re , and does not depend strongly on acceleration.



Error Bars for the Con simulations are two standard deviations large from the mean. Reynolds number values determined using $L = 1$.

Figure 10. Log_{10} of the Okubo Weiss Parameter over Reynolds Number

B. THERMAL PERTURBATIONS

Thermal wake signatures can persist for many hours (Benbow 2016) and have been found to increase in magnitude with increased SB velocity (Martin 2016). Thus, the growth of thermal signatures is an excellent diagnostic to determine the presence of acceleration. For accelerating SBs, the wakes are composed of younger near-wake regions characterized by higher Re and older intermediate- to late-wake regions with lower Re . Hence, the accelerating SBs wakes should have temperature perturbation signatures that are a hybrid of those produced by SBs with a range of constant velocities.

Analyses were conducted only on the most mature wake signatures downstream of the SB in the model volume where the SB position is close to $x_{SB} \approx 30$, without exiting the model volume. To focus the study on these downstream wake signatures, the maximum temperature perturbation and integrated energy analyses are conducted with a mask on the

raw data. In Figure 11, the mask is composed of the volume in front of the sphere as described by

$$x > x_{SB}, \quad (3.5)$$

and the volume surrounding the sphere is described by

$$(x - x_{SB})^2 + (y - y_{SB})^2 + (z - z_{SB})^2 < 1. \quad (3.6)$$

This neglects the upstream wake, the non-wake values of the SB itself, and minimizes the signal due to internal wave reflections on the $x = 30$ boundary.



Figure 11. Mask Configuration of the Model Volume

The raw temperature data is smoothed using a moving mean with window size of 15 grid cells. From the smoothed data (T_{smooth}), the background temperature field is determined for each vertical layer ($\bar{T}(z)$). These mean temperatures are subtracted from the smoothed temperature data to produce perturbation temperatures (T') as described by

$$T' = T_{smooth} - \bar{T}(z). \quad (3.7)$$

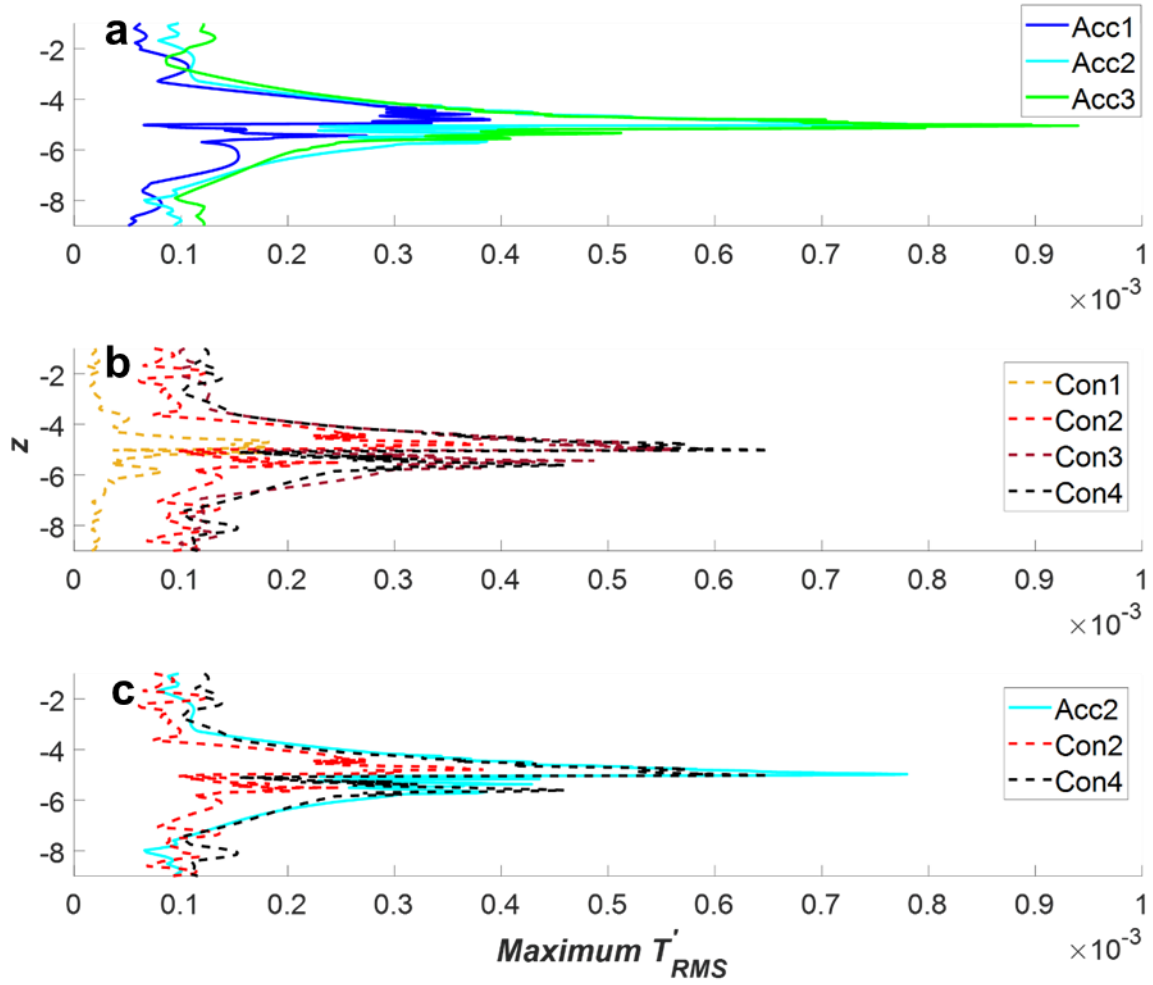
The root mean square temperature perturbations (T'_{RMS}) data are calculated by

$$T'_{RMS} = \sqrt{(T')^2}. \quad (3.8)$$

In Figure 12, the vertical profile of maximum T'_{RMS} values are plotted just before the SB exits the model volume. This allows for mature constant velocity wakes to be compared with accelerating wakes produced by accelerating SBs having traveled similar

distances. The highest maximum T'_{RMS} signatures are seen at the depths of the SB's propagation and initial wake creation ($z = [-4.5 -5.5]$) and is the region with the strongest turbulence. The thermal signatures gradually decrease outwards to the vertical wings of the wake ($z < -8$ and $z > -2$), as the initial perturbations weaken sufficiently allowing the surrounding fluid's restoring forces to begin restratification and are indicative of internal waves. The maximum T'_{RMS} values for the central wake region and the wake wings are listed in Table 3.

In Figure 12a-b, with increasing acceleration or constant velocity there are increasing maximum T'_{RMS} signatures. For the accelerating cases, their central wake signatures are proportionally larger than the wing signatures. The constant velocity cases have less pronounced central wake signatures as compared to their wake wings. From the thermal signature values in Table 3 and Figure 12c, the Acc case has higher but comparable central wake signatures to Con4 but has wake wing signatures more comparable to the Con2. Thus, the accelerating cases exhibit central wake behavior similar to Con cases with the same velocity of the SB, while having wake wing behavior similar to Con cases having half their SB's velocity. This leads to a pointed distribution shape of thermal signatures for the Acc cases, while the Con cases have a broader, less pointed distribution shape for their signatures. For the Acc cases, the thermal signature distribution in the central wake matches prior vorticity observations, where their stronger and more coherent vortices concentrates their thermal signatures in the central wake. Whereas the Con cases, have weaker, less numerous, and less coherent vortices allowing the thermal signatures to diffuse further more toward the wake wings and create a broader wake signature distribution. These thermal signature distributions could theoretically be detected by spatially separated sensors and detect the presence of acceleration from the SB's wakes.



The maximum T'_{RMS} values are taken at the last time step before the SB leaves the model volume. The accelerating (a) and constant velocity cases (b) are plotted separately, and Acc2, Con2, and Con4 cases are plotted together (c).

Figure 12. Maximum Vertical T'_{RMS}

Table 3. Maximum T'_{RMS} Values

Case	Acc1	Acc2	Acc3	Con1	Con2	Con3	Con4
Max T'_{RMS} in central wake (1×10^{-4})	3.89	7.80	9.40	1.83	3.83	5.65	6.51
Max T'_{RMS} in the wake wings (1×10^{-4})	.82	1.09	1.49	.296	1.25	1.34	1.53

Central wake is defined as $z = (-2 - 8)$. Wake wings are defined as $z < -8$ and $z > -2$.

C. WAKE AREA

To study the wake's size, to include its growth and decay, a quantitative parameter is needed. Several time series of the vertical cross sections of the wakes were taken at where the velocities of the accelerated SBs match the velocities of the Con cases as shown in Figure 13. This allows for a comparative time evolution of the wake size via the wake's area in this slice. The time of the SB crossing the cross section in each case is denoted t_{cross} . Cross sections for the Con cases are similarly taken at $x = 7$ (70m), $x = 14$ (140m), $x = 21$ (210m) and $x = 28$ (280m) points, to obtain multiple samples of the wake lifecycle. The presence of the wake is determined at each grid cell of the vertical cross section if the root mean square temperature perturbations (T'_{RMS}) surpassed the temperature threshold of $T'_{\text{RMS}} > 1 \times 10^{-5}$ (4.67e-2°C). The areas of each grid cell were summed to determine the area of the wake over time.

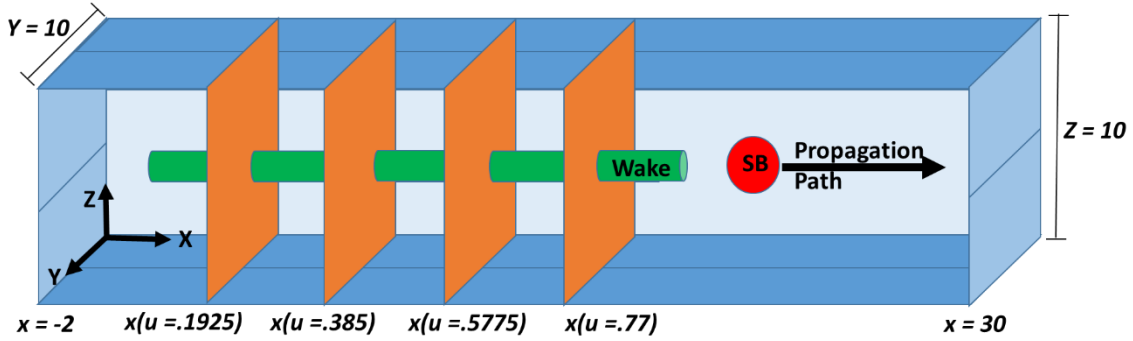
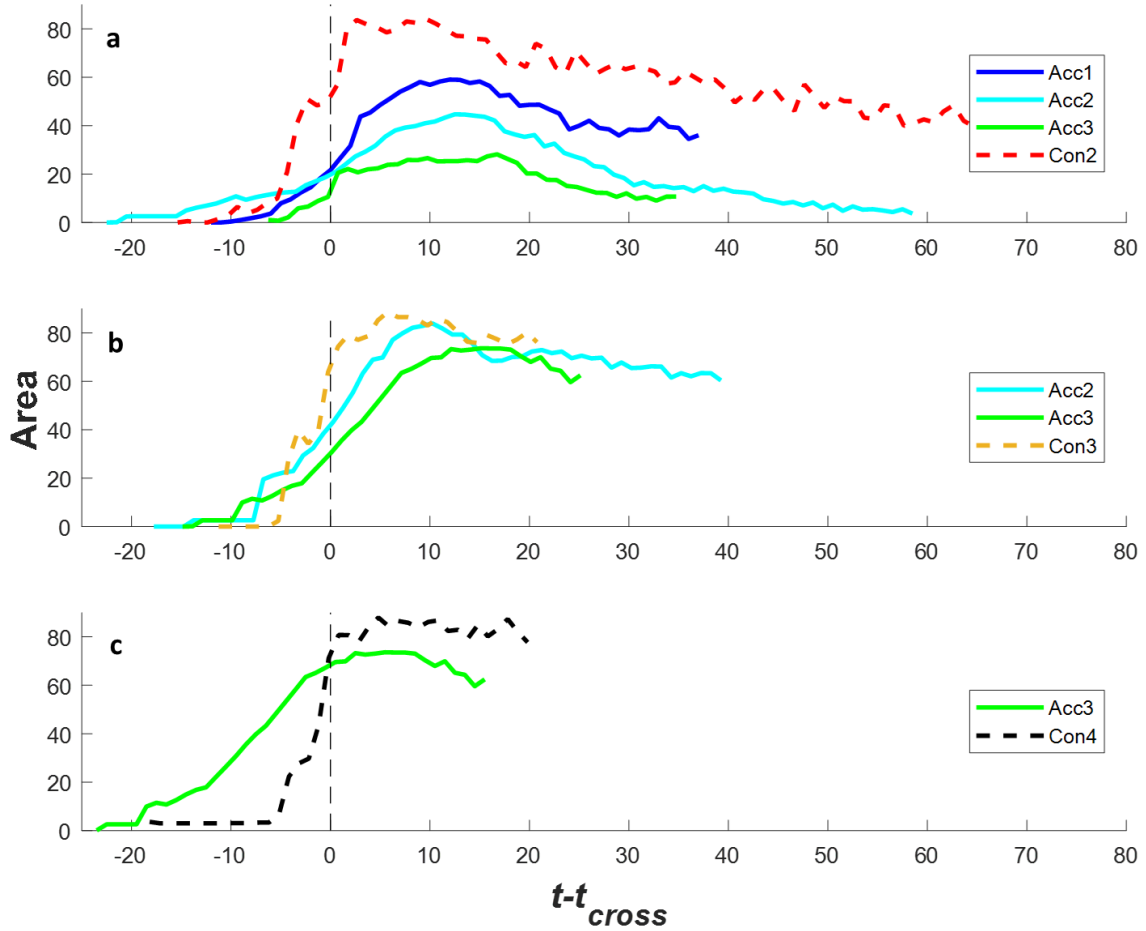


Figure 13. Vertical Cross Section Configuration to Determine Wake Area

Figure 14 compares the wake area evolution of the accelerating cases with the Con2, Con3, and Con4 cases. The constant velocity wake areas are measured at $x=16$, to view a mature wake without initial startup transients, while allowing sufficient run time to follow the area's evolution after the SB's passage. The wake areas upon passage of the SB, the maximum wake areas, and the times to achieve the maximum area are listed in Table 4. All the constant velocity cases show sharply growing wake areas before the SB crosses at $t - t_{\text{cross}} = 0$. The growing area before the SB crosses corresponds to the upstream wake

where fluid ahead of the moving body is pushed and similarly moving along with the SB. A similar sharply sloped area growth occurs immediately after passage of the SB. As the SB velocity increases from Con2–4, the wake areas at SB crossing, and maxima correspondingly increase, and the time required to achieve the maxima decreases.



Shown are the transverse cross-sectional wake areas for Acc cases at $x(u=.385)$ (a), $x(u=.5775)$ (b), and $x(u=.77)$ (c). The Con cross sections were at $x=16$. The times are centered $t-t_{cross}$ where the black dashed line represents the time when the SB's center crosses that x position.

Figure 14. Wake Area over SB Crossing Time ($t-t_{cross}$) for $T'_{RMS} > 1.0 \times 10^{-5}$

For all Acc cases, there is a more gradual increase in wake area upstream of the SB that is detected much earlier. At SB crossing, the Acc1–3 areas only reach to 25–42% of Con2's area. As velocities increase, the percentage of Acc areas to Con area likewise

increases for Acc2 and Acc3 to 55–64% of Con3, and for Acc3 to 88% of Con4. After passage of the SB, the Acc wake areas continue to gradually increase until a maximum is reached at approximately $t=10$ – 16 (10-16s) in Figures 15a–b and $t=5.5$ (5.5s) in Figure 14c, both times are longer than their matching Con cases. The Acc area maxima are also smaller than the matching Con areas, between 34–71% of Con2’s area, 86–95% of Con3’s area, 84% of the Con4’s area. These wake area findings also correlate to prior vorticity results similarly to the maximum T'_{RMS} findings. The Acc cases have stronger and more coherent vortices initially concentrating the wake into a smaller area, reducing the maximum area, and increasing the time to achieve the maximum area.

Table 4. Wake Areas at SB Crossing and at Maximum

	SB Velocity	Simulation					
		Con2	Con3	Con4	Acc1	Acc2	Acc3
Area at SB Crossing	$u=.385$	52.0			22.0	19.6	13.0
	$u=.5775$		67.0			42.0	30.0
	$u=.77$			73			68.4
Max Area	$u=.385$	83.6			59.0	44.7	28.2
	$u=.5775$		88.6			83.9	73.6
	$u=.77$			88			73.6
Time to achieve Max Area (s)	$u=.385$	2.6			12.0	12.5	16.8
	$u=.5775$		5.8			10.3	15.1
	$u=.77$			4.8			5.5

Comparing only the Acc cases, for a given velocity the systems with lower acceleration have faster area growths, larger area maxima than those with faster larger accelerations. The constant velocity cases, those with no acceleration, are consistent with this trend, as they have the fastest area growths, and largest area maxima. This observation agrees with the vorticity profiles, with higher accelerating cases having narrower wakes across the same distance traveled. The prior vorticity argument, where higher accelerations, with higher vorticities concentrate their wakes into smaller areas that do not wander as far from their origin as compared to the slower accelerating cases.

At higher Re , there appears to be a positive correlation between acceleration and upstream wake area (Figure 14c). These larger upstream wakes of the accelerating cases protrude further ahead of the SB than the shorter and blunter upstream regions of the constant velocity cases. As the body accelerates, there needs to be an increasing volume of water displaced in the upstream region, leading to the growth of upstream wake with increasing acceleration. This upstream wake behavior at differing turbulent regimes is an area for further study

Accelerating SBs produce wakes with smaller vertical cross sectional areas as compared wakes produced with no acceleration. The presence of acceleration increases the magnitude of vorticity present, which concentrates the wake signatures within the vortices. The accelerating SB has an increasing volume of displaced fluid in the upstream region, which creates a pronounced upstream wake. This concentration of the signatures near the central wake creates a pointed wake shape. SBs under constant velocity have lower vorticity signatures, which are weaker and allow for the wake signatures to diffuse more throughout the water column leading to a broader wake shape immediately behind the SB. These differing wake sizes and shapes can be detected in the ocean through a network of spatially separated sensors, which can determine the presence of acceleration or not of a SB.

D. INTEGRATED ENERGY

To see the combined effects of thermal, and velocity perturbations like vorticity on the wake signature, total energy (E) is investigated. The total energy is determined by integrating the following:

$$E = \int \frac{\mathbf{u}^2}{2} - (T')^2 T_{0z}^{-1} dV, \quad (3.9)$$

where T_{0z} is the initial background temperature field. In Figure 15, the total integrated energy (E) is plotted over distance traveled by the SB (x_{SB}) up until the SB exits the domain ($x_{SB} \approx 30$ (300m)), and the final energies are listed in Table 5. By the time the SB has passed through the entire domain, the accelerating SBs have imparted more energy into the system than their mean velocity equivalents, with Acc2 having 36% more energy than

Con2. While the increase in E seems exponential, the increase is not as large as the growth of the previous vorticity values, therefore vorticity can contribute but cannot fully explain the growth in energy. Instead as energy is the traditional integral measure of velocity, there needs to be a region of the wake increasing in velocity similarly to the E plots. The prior upstream wake area plots have a plausible relation to the increased E . As the accelerating bodies reach higher velocities, they displace an increasing volume of water that will also move at the speed of the SB. The larger upstream wake areas of the accelerating cases can be vessels for the observed higher E . Additionally as the constant velocity cases have linearly growing E but have near steady vorticity values, this could indicate the spreading and diffusing of the thermal signatures through the model volume, and another contributor to the E growth.

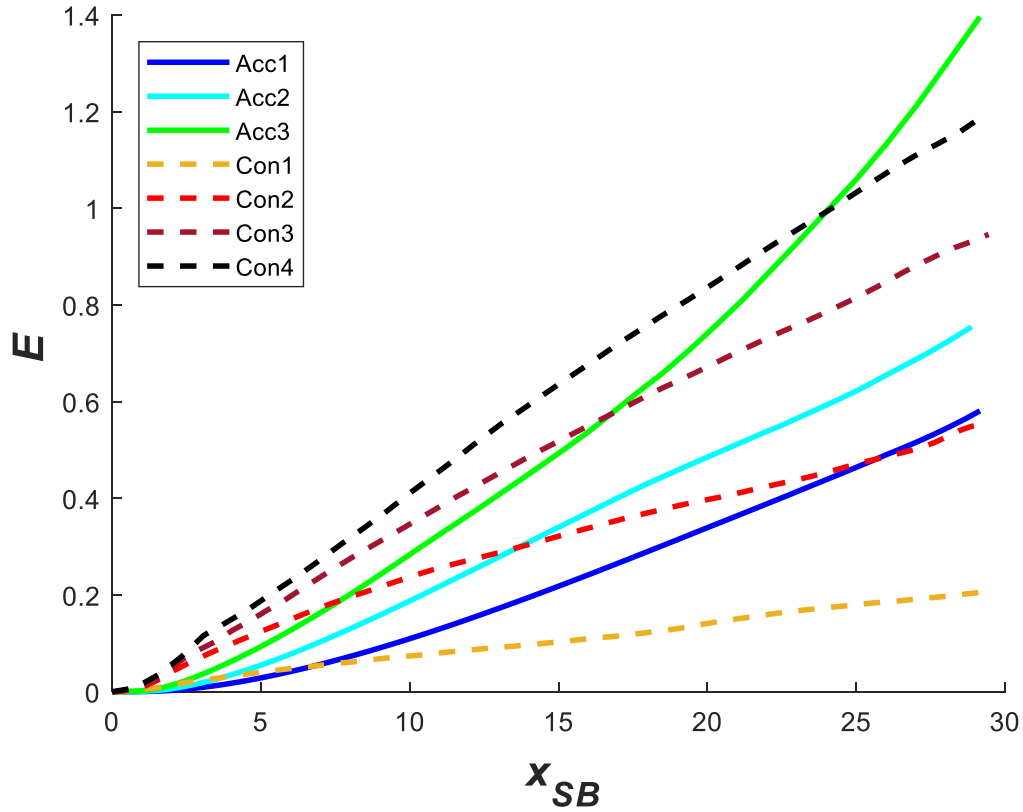
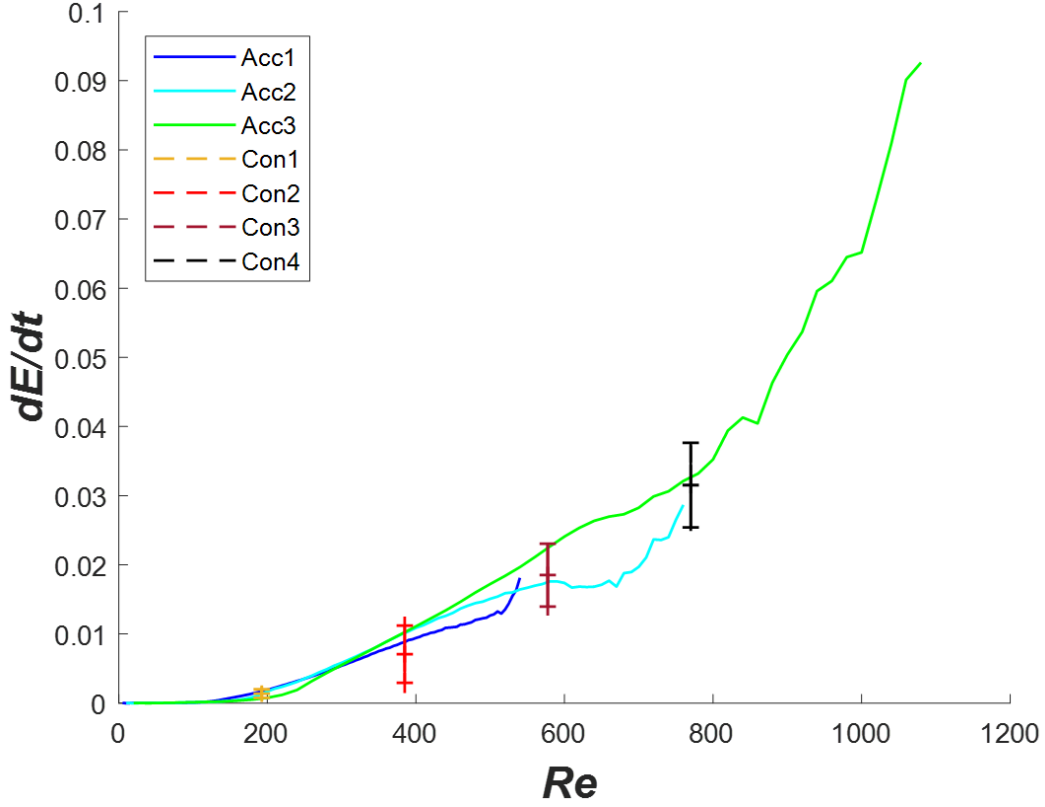


Figure 15. Total Integrated Energy (E) over Distance Traveled (x_{SB})

Table 5. Integrated Energy Values across the Same Distance Traveled

Simulation	Acc1	Acc2	Acc3	Con1	Con2	Con3	Con4
E at $x \approx 30$.58	.75	1.40	.21	.55	.95	1.19

To better compare the E injection rates of the Acc cases propagating at the corresponding Con cases SB velocity, the rate of change of E with regard to time (dE/dt) is plotted according to Reynolds number in Figure 16. Under these dE/dt ranges, the dE/dt for the Acc cases does not vary significantly from the four Con cases. Thus, the injection rate of total energy by a SB into the surrounding environment appears to depend only on Re and is independent of the acceleration. But as the shape of the wake signatures differs between the accelerating and constant velocity cases, the E injection rate can be presumed to be concentrated near the central wake in the region with the greatest number of vortices, and in the larger upstream wake region for the accelerating cases. And for the constant velocity cases, their similar E injection is spread across a more diffused, and broader wake area.



Error Bars for the Con simulations are two standard deviations away from the mean.
Reynolds number values determined using $L = 1$.

Figure 16. Energy Rate of Change over Reynolds Number

To isolate the decay rate, the total integrated energy E is calculated for the Acc2 and Con2 cases after the SB has left the model volume and is no longer injecting E into the system. The temporal evolution of E is fitted to the following:

$$E = E_0 e^{(bt)}, \quad (3.10)$$

where E_0 is the initial value after the SB exits the domain, and b is the exponential decay rate over time. Fitted curves are plotted in Figure 17 along with the original data. The exponential decay rate for Acc2 is found to be half that of Con2 ($b_{\text{Acc2}} = -0.005635$ versus $b_{\text{Con2}} = -.011$). The energy decay rate is slower for the accelerating cases. This supports the previous visual vorticity observations of Acc2 having stronger more coherent vortices that decay at a slower rate than the weaker and loss coherent vortices of Con2. Acc2's slower decay rate in conjunction with the result that Acc2 produced 36% higher E than Con2 across the same distance traveled, suggests that the accelerating cases will have higher E

wake signatures that persist for much longer than E signatures produced by constant velocity cases. Further study is needed beyond the two simulations presented here to confirm this phenomenon.

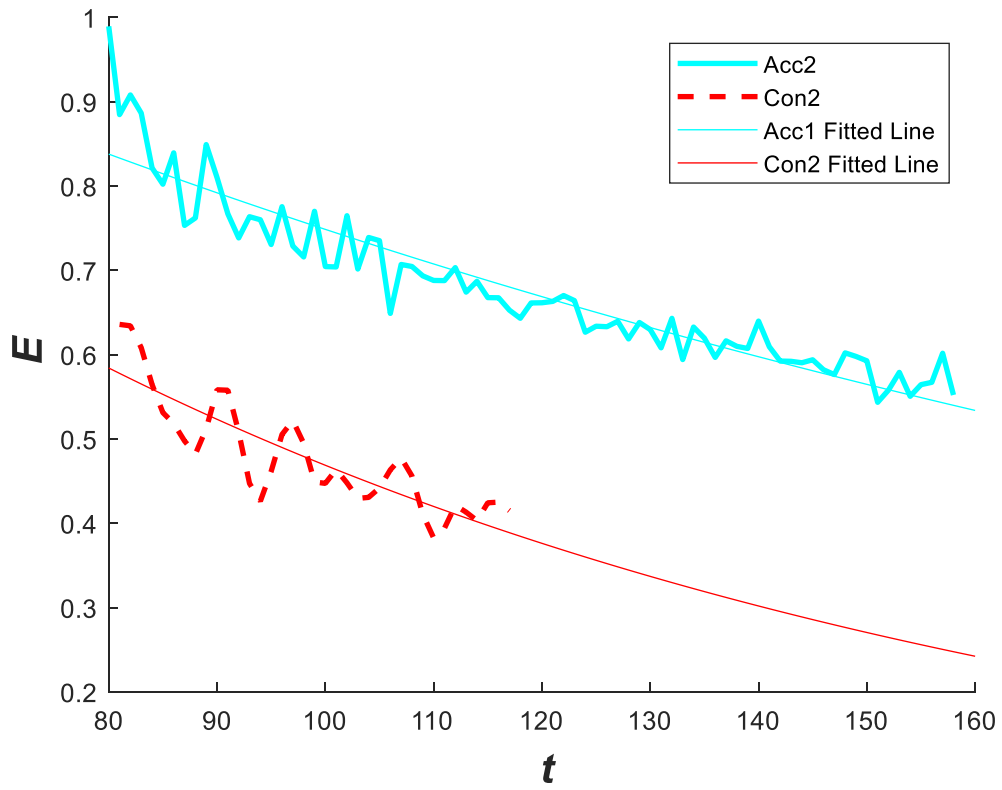


Figure 17. Energy Decay over Time with Fitted Curves

THIS PAGE INTENTIONALLY LEFT BLANK

IV. DISCUSSION

A. CONCLUSIONS

This study models the wake signatures of towed spherical submerged bodies under the effects of either acceleration or constant velocity traveling through a stratified fluid. The persisting wake signatures of vorticity, temperature, and energy are considered, as these are the most likely candidates for detection operationally. The vorticity and energy perturbation injection rates are found to be comparable between the accelerating and constant velocity cases. The injection rates depend solely on Re and are independent of acceleration.

When comparing the wake signatures produced by accelerating and non-accelerating SBs that have traveled across the same distance, there are considerable differences in wake size, shape, and perturbation strengths. With higher amounts of vorticity present in the accelerating cases, there are stronger, more coherent vortices present. As seen in the maximum temperature perturbation and wake area results, these vortices concentrate the thermal signatures around the central wake, and leads to the creation of a pointed wake shape. Theoretically, these vortices can also concentrate other perturbation signatures into similar pointed wake shapes, such as salinity. In contrast, the constant velocity cases have lower vorticity, allowing their thermal signatures to diffuse, and creating broader wake shapes and perturbation profiles.

The total energy present in the system grows exponentially for accelerating cases, while growing linearly for the constant velocity cases. As the total energy for the constant velocity cases does not reach an equilibrium similarly to the Okubo Weiss parameter, this indicates there is a continued increase and spreading of the thermal perturbations. This finding is supported with previous thermal signature studies with the submerged wake's thermal perturbations spreading toward the water surface (Benbow 2016, Martin 2016, Moody et al. 2016). The higher energy finding can also be captured with the increasing size of the upstream wake with higher accelerations, and further contributes to the pointed shape of the accelerating cases. These differing wake shapes are easily discernable in this

study's vorticity, thermal, and energy-based signatures, and can be used to determine the presence of acceleration or constant velocity in the wake producing body.

This study finds, there are detectable vorticity and thermal based signature differences between stratified wakes produced by accelerating and non-accelerating SBs. The differences in thermal signatures continues to expand our level of knowledge of stratified wake morphology, and further supports the growing field of non-acoustic or more specifically the thermal based detection of submerged vessels. The finding for increased vorticity is particularly exciting as the vortices can be measured acoustically via Acoustic Doppler Current Profilers (ADCPs). And opens the avenue of indirect acoustic detection of submerged vessels with the detection of their wakes. Altogether, stratified wake signatures can be used under the concept of hybrid detection, the use of both acoustic and non-acoustic detection of submarines.

B. OPERATIONAL RELEVANCE

The stratified wake signatures of submarines cannot be hidden in the same manner as their acoustic signatures. Any submarine moving at speed will produce a wake, which can persist from hours to days. These wakes can be detected can build historical locations of submerged bodies. Several modern ASW sensors such as sonobuoys and unmanned underwater vehicles are often deployed in groups and layered or gridded together to pinpoint tracks of interest. These networks of sensors can be equipped with vorticity sensors such as ADCPs and thermal sensors, and they are already deployed in networks ideally located to spatially and temporally detect and determine the shape and magnitudes of the wakes produced stratified submerged vessels. With the future development of more sensitive temperature and vorticity sensors and field experiments the minute values of the wake perturbations can be detected at even longer ranges and greater time periods. Fieldwork producing empirical values for the wake perturbations can be obtained to determine the passage of a submerged body, identify its size, speed, and presence of acceleration. This can be used to predict the future location of the submerged bodies. These results will allow ASW assets to more accurately detect, locate, and predict the track of submarines.

C. FUTURE RESEARCH

As this study pertains to the use of direct numerical simulations, these results are best validated with a field study testing similar parameters. This study's model runs can be extended to further study the decay behavior in the late wake regime, especially the change in magnitude, movement, number, size, and separation distances of the late wake vortices. The model configuration can also be modified to analyze the wakes produced by decelerating SBs. Alternatively, this study can be replicated using self-propelled bodies vice towed bodies to investigate the effects of momentum being injected into the system especially if the simulation models the effects of propeller-induced turbulence (de Stadlar and Sarkar 2013, Brucker and Sarkar 2010). To better study the near and intermediate wakes of constant and accelerating bodies, the bluff body sphere should be replaced with an ellipsoid shape similar to modern undersea going vessels such as submarines or unmanned underwater vehicles. Of all these possible topics, this study's findings on acceleration's effects are merely the foundation for the future DNS investigation of the effects of turning and maneuvering.

THIS PAGE INTENTIONALLY LEFT BLANK

LIST OF REFERENCES

- Benbow, T. A., 2016: The effects of double diffusion and background turbulence on the persistence of submarine wakes. Master's thesis, Dept. of Oceanography, Naval Postgraduate School, 25 pp.
- Bessel, F. W., 1828: Investigations on the length of the simple seconds pendulum. *Treatises of the Academy of Berlin*, 254 pp, <http://doi.org/10.3931/e-rara-46652>.
- Lin, J. T., Y. H. Pao, 1979: Wakes in stratified fluids: A review. *Annual Review of Fluid Mechanics*, **11**, 317–338, <https://doi.org/10.1146/annurev.fl.11.010179.001533>.
- Lorfeld, D. J., 2017: The effects of earth's rotation on the late submarine wake. Master's thesis, Dept. of Oceanography, Naval Postgraduate School, 27 pp.
- Marshall, J., C. Hill, L. Perelman, and A. Adcroft, 1997: Hydrostatic, quasi-hydrostatic, and nonhydrostatic ocean modeling. *Journal of Geophysical Research: Oceans*, **102**, 5733–5752; <https://doi.org/10.1029/96JC02776>.
- Martin, M. A., 2016: Influence of momentum excess on the pattern and dynamics of intermediate-range stratified wakes. Master's thesis, Dept. of Oceanography, Naval Postgraduate School, 91 pp.
- Merriam, C. J., 2015: Laboratory experiments on stratified wakes. Master's thesis, Dept. of Oceanography, Naval Postgraduate School, 57 pp.
- Meunier, P., and G. R. Spedding, 2004: A loss of memory in stratified momentum wakes, *Physics of Fluids*, **16**, 298–305 pp.
- Mitkin, V. V. and Y. D. Chashechkin, 2000: Experimental Investigation of the Velocity Field near a Cylinder in a Continuously Stratified Fluid. *Fluid Dynamics*, **35**, 642–651.
- Moody, Z. E., C. J. Merriam, T. Radko, and J. Joseph, 2017: On the structure and dynamics of stratified wakes generated by submerged propagating objects. *Journal of Operational Oceanography*, **10**, 191–204.
- Newman, T. P., 2014: Surface signatures of submerged bodies propagating in stratified fluids. Master's Thesis, Department of Oceanography, Naval Postgraduate School, 59.
- Pao, H. P., and T. W. Kao, 1977: Vortex structure in the wake of a sphere. *Physics of Fluids*, **20**, 187–191 pp, <https://doi.org/10.1063/1.861854>.

- Spedding, G. R., 1997: The evolution of initially turbulent bluff-body wakes at high internal Froude number. *Journal of Fluid Mechanics*, **337**, 283–301, <https://doi.org/10.1017/S0022112096004557>.
- Spedding, G. R., 2002: Vertical structure in stratified wakes with high initial Froude number. *Journal of Fluid Mechanics*, **454**, 71–112. <https://doi.org/10.1017/S0022112001007182>.
- Spedding, G. R., 2014: Wake signature detection. *Annual Review of Fluid Mechanics*, **46**, 273–302, <https://doi.org/10.1146/annurev-fluid-011212-140747>.
- Voropayev, S. I., G. B. McEachern, H. J. S. Fernando, and D. L. Boyer, 1999: Large vortex structures behind a maneuvering body in stratified fluids. *Physics of Fluids*, **11**, 1682–1684, <https://doi.org/10.1063/1.870030>.
- Vortmeyer-Kley, R., U. Gräwe, and U. Feudel, 2016: Detecting and tracking eddies in oceanic flow fields: A Lagrangian descriptor based on the modulus of vorticity. *Nonlinear Processes in Geophysics*, **23**, 159–173, <https://doi.org/10.5194/npg-23-159-2016>.

INITIAL DISTRIBUTION LIST

1. Defense Technical Information Center
Ft. Belvoir, Virginia
2. Dudley Knox Library
Naval Postgraduate School
Monterey, California